

Journal of Materials Chemistry A

Materials for energy and sustainability

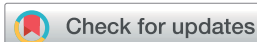
rsc.li/materials-a



ISSN 2050-7488

PAPER

Huagui Nie, Zhi Yang *et al.*
Intermolecular electron modulation by P/O bridging in
an IrO₂-CoPi catalyst to enhance the hydrogen evolution
reaction

Cite this: *J. Mater. Chem. A*, 2020, **8**, 8273

Intermolecular electron modulation by P/O bridging in an IrO₂-CoPi catalyst to enhance the hydrogen evolution reaction†

Xiannuo Zheng,^{‡a} Huagui Nie,^{*a} Yingxin Zhan,^a Xuemei Zhou,^a Huan Duan^b and Zhi Yang^{ib*}

Development of a highly efficient electrocatalyst for the hydrogen evolution reaction (HER) remains a great challenge. Herein, a catalytic system is constructed based on a low content of atomically dispersed iridium oxide (IrO₂) coordinated with cobalt phosphate (CoPi) onto carbon nanotubes (CNTs) by a two-step electrochemical deposition procedure. The resultant IrO₂-CoPi-CNT catalytic system with a low loading of Ir (0.41 wt%) has Pt-like performances with a small overpotential of 29 mV at a current density of 10 mA cm⁻² and a low Tafel slope of 27 mV dec⁻¹ towards the HER. X-ray photoelectron spectroscopy (XPS) measurements and density functional theory (DFT) calculations reveal that the electronic structure of CoPi and IrO₂ can be effectively modulated through electron-donating phosphate bonds (P/O bridging), thus giving a more favorable ΔG_{H^*} with a value of -0.13 eV. These bonds also prevent IrO₂ from undergoing further aggregation. Besides, CoPi can rapidly cleave HO-H bonds and transfer an abundance of H* intermediates to nearby IrO₂ catalytic sites, facilitating the formation and release of H₂ molecules. This work manifests the importance of the electron structure of catalysts in electrocatalysis and provides an avenue for preparing highly active electrocatalysts towards the HER.

Received 17th January 2020
Accepted 26th February 2020

DOI: 10.1039/d0ta00703j

rsc.li/materials-a

Introduction

The hydrogen evolution reaction (HER) in the electrolysis of water is an economical, eco-friendly and efficient approach to produce high-purity hydrogen.¹⁻⁴ The catalytic activity of HER catalysts is often theoretically described by the Gibbs free energy of hydrogen (ΔG_{H^*}).⁵ To date, platinum (Pt) and its alloys, which have a near-zero ΔG_{H^*} , are considered to be the most active catalysts for the HER.^{6,7} However, the scarcity and high cost of Pt greatly restrict its commercialization.⁸⁻¹⁰ Therefore, reducing Pt usage and developing Pt-free catalysts are important approaches to overcome the challenges in achieving cost-effective hydrogen production.¹¹⁻¹⁴

Recently, transition-metal phosphides have been shown to possess tremendous potential as alternatives to Pt.¹⁵ These material systems have been widely studied in the HER owing to their cost-effectiveness, specific electronic structure, and high natural abundance of the constituent elements.^{16,17} Density functional theory (DFT) calculations have suggested that P sites in transition-

metal phosphides can directly participate in the HER and have moderate bonding to intermediates, which is a rate-limiting step in hydrogen production.¹⁸ To further improve the electrochemical performance of transition-metal phosphides, some groups have used amorphous transition-metal phosphate (TMPi) materials owing to their impressive intrinsic properties.¹⁹⁻²² However, these materials are susceptible to corrosion in acidic electrolytes, which leads to a rapid decrease of their activity. Furthermore, the electrocatalytic performances of TMPi toward the HER are not yet comparable to those of noble-metal based catalysts.²³⁻²⁵ Hence, it is still critically challenging to improve the performances of amorphous TMPi-based electrocatalysts for the HER.

The Sabatier principle reveals a crucial correlation between the activity of catalysts and the hydrogen adsorption energy in the HER.²⁶ For efficient HER catalysts, the adsorption energy should be neither too high (*i.e.*, slow adsorption) nor too low (*i.e.*, slow desorption), otherwise the overall rate is slow.²⁷ A volcano plot shows the connection between the HER activity at the onset potential and the hydrogen adsorption ΔG_{H^*} .²⁸ As expected from the volcano plots, iridium (Ir) is considered to be a potential catalyst for the HER.²⁹ However, Ir-based catalysts have not been extensively used, which might be attributed to the fact that Ir atoms/clusters tend to aggregate. Cobalt phosphate (CoPi) has been theoretically calculated to have a low energy barrier for adsorption of hydrogen atoms and is regarded as a potential catalyst for the HER.^{30,31} Notably, chemical coupling into a uniform hybrid of Ir and CoPi might achieve the desired

^aKey Laboratory of Carbon Materials of Zhejiang Province, Wenzhou University, Wenzhou 325035, China. E-mail: huaguinie@126.com; yang201079@126.com

^bSchool of Chemistry and Chemical Engineering, Southwest University, Chongqing, China

† Electronic supplementary information (ESI) available. See DOI: 10.1039/d0ta00703j

‡ These authors contributed equally to this work.

adsorption–desorption behavior ($|\Delta G_{H^*}| \rightarrow 0$) to facilitate the HER kinetics.³² However, there has been little research on CoPi combined with noble metals for the HER to date.

Results and discussion

Structural analysis of the IrO₂-CoPi-CNT hybrid catalyst

In the present study, the IrO₂-CoPi-CNT catalyst was synthesized through a two-step electrochemical deposition procedure (see the Experimental section for details in the ESI†). First, a CNT-modified glass carbon electrode (GCE) was immersed in cobaltous phosphate solution and a deposition was performed through cyclic voltammetry (CV) to obtain the hybrid catalysts. The performances of the samples, formed over different numbers of deposition cycles, in the HER are shown in Fig. S1

(ESI†). The sample treated with 30 cycles of CV had the highest catalytic current. We denote this sample as CoPi-CNTs and used it in subsequent experiments. Second, the CoPi-CNT electrode was used as the working electrode and repeated CV scans were performed with an Ir wire as a counter electrode in 0.5 M H₂SO₄. The effects of the deposition cycles on the performance in the HER with a graphite counter electrode are shown in Fig. S2 (ESI†). The best performance was achieved after 12 000 cycles and the corresponding sample is denoted as IrO₂-CoPi-CNTs. Additionally, control experiments without CoPi decoration were performed through a second synthesis procedure and this sample is denoted as IrO₂-CNTs.

The obtained catalysts were further characterized by scanning electron microscopy (SEM) and transmission electron microscopy (TEM) imaging. From Fig. 1a, S3 and S4 (ESI†) for

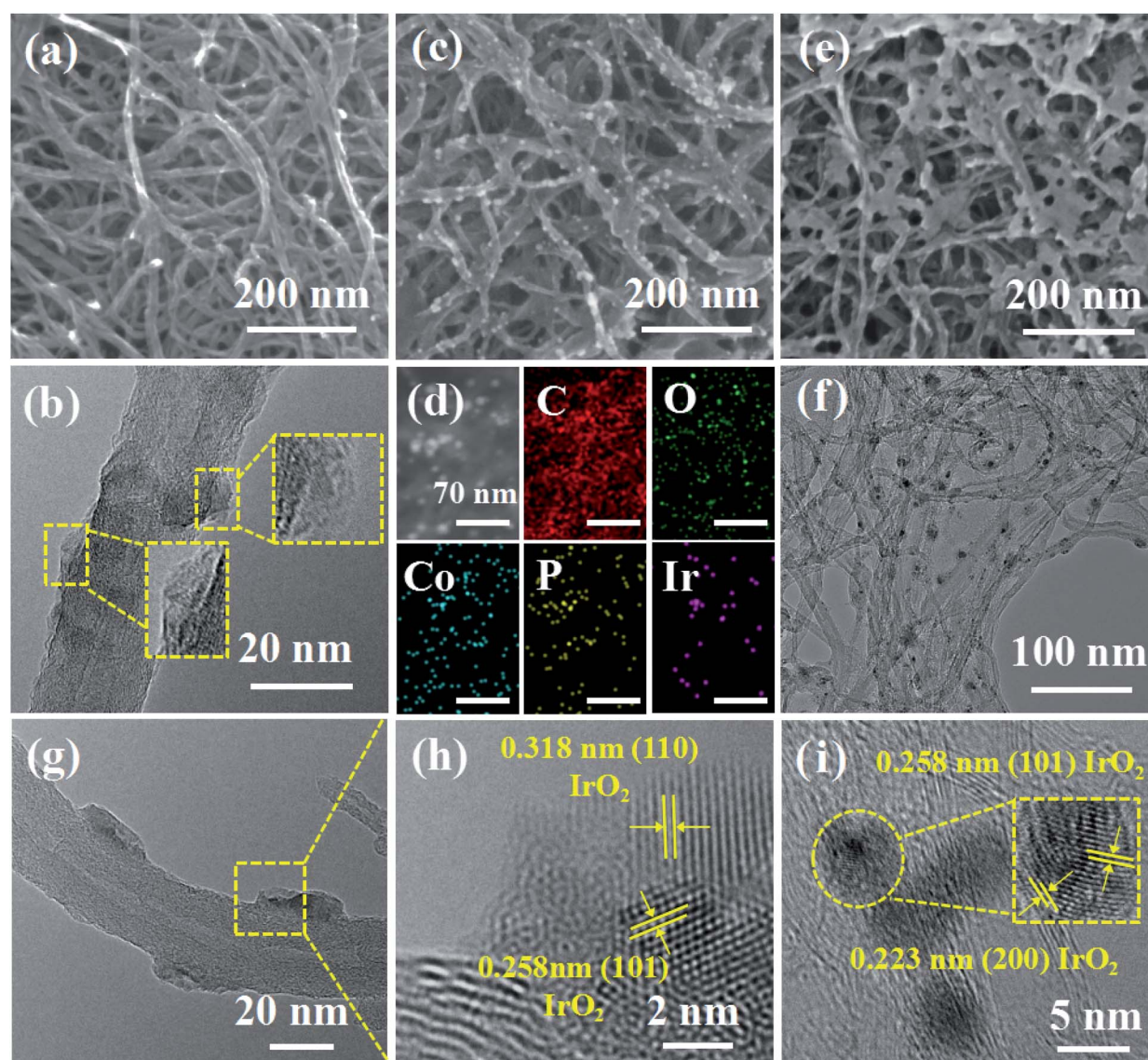


Fig. 1 Characterization of the hybrid catalysts. (a) SEM and (b) HRTEM images of the CoPi-CNT hybrid catalyst. (c) SEM image of the IrO₂-CoPi-CNT hybrid catalyst. (d) STEM and EDS elemental mapping images of C, O, Co, P, and Ir for the IrO₂-CoPi-CNT hybrid catalyst. (e) SEM images of the IrO₂-CNT hybrid catalyst. (f and g) TEM and (h and i) HRTEM images of the IrO₂-CoPi-CNT hybrid catalyst; the inset of (i) shows high-resolution lattice fringes.

the CoPi-CNT catalyst, we observed that the CNTs coarsened and became thicker as the number of deposition cycles was increased. The high-resolution TEM (HRTEM) image in Fig. 1b also shows an amorphous coating over the CNTs. Bright spots of the as-prepared IrO₂-CoPi-CNT catalysts were homogeneously distributed over the material (Fig. 1c, and S5 in the ESI†).

The particles become larger as the number of deposition cycles increased. Observations from scanning TEM (STEM) and energy dispersive X-ray spectroscopy (EDS) elemental mapping images of C, O, Co, P, and Ir in the IrO₂-CoPi-CNT hybrid catalyst (Fig. 1d) further confirmed that the bright spots were composed of Ir, Co, P, and O. Conversely, the IrO₂-CNT catalyst tended to aggregate (Fig. 1e, S6 and S7 in the ESI†) as the content increased. The fine structure of the IrO₂-CoPi-CNT catalyst was explored, and the TEM images in Fig. 1f and g and the HRTEM images in Fig. 1h and i show two phases: one is an amorphous phase and the other consists of distinct lattice fringes. The crystal lattice fringe spacings of 0.318, 0.258 and 0.223 nm represent the (110), (101) and (200) planes of IrO₂, respectively. These results indicate that CoPi promotes an even distribution of IrO₂ on the CNT support. Inductively coupled plasma optical emission spectroscopy (ICP-OES) suggested that the IrO₂-CoPi-CNT samples had an Ir loading of 0.41 wt%.

X-ray photoelectron spectroscopy (XPS) further verified the presence and the electronic states of IrO₂ in the IrO₂-CoPi-CNT catalyst. As shown in Fig. 2a, two spin-orbit doublets were observed in the high resolution XPS spectra of Co 2p in IrO₂-CoPi-CNTs, which are assigned to Co 2p_{3/2} and Co 2p_{1/2}. Their binding energies (BEs) slightly shifted to higher field compared with those of CoPi-CNTs. The fitted Co 2p spectrum of the IrO₂-CoPi-CNT sample was assigned to Co³⁺ (780.0 and 795.6 eV), Co²⁺ (781.6 and 797.5 eV), and satellite peaks (786.1 and 803.2 eV), respectively.^{33,34} A much higher intensity ratio of Co²⁺/Co³⁺ was found after combination with IrO₂. Importantly, the spectra of P 2p in Fig. 2b showed a phosphate peak, and the P-O bonding energy positively shifted from 133.3 to 134.6 eV, indicating the electron donating ability of P.³⁵ In contrast, the Ir 4f peaks (Fig. 2c) of IrO₂-CoPi-CNTs slightly negatively shifted compared with those of IrO₂-CNTs. The fitted Ir 4f spectrum corresponds to Ir⁴⁺ (peaks at 63.2 and 66.1 eV) and Ir³⁺ (peaks at

62.3 and 65.2 eV).²⁹ The change from Ir⁴⁺ to Ir³⁺ in the IrO₂-CoPi-CNT catalyst indicates that more lower-valence IrO₂ was produced by bridging with CoPi. Low-valence Ir sites indicated a slightly enhanced hydrogen binding ability.³⁶ Hence, the XPS results suggest that the Co or Pi groups in the IrO₂-CoPi-CNTs donate electrons to IrO₂. Such a modulation of the electronic structure might significantly enhance the electrocatalytic activity of the IrO₂-CoPi-CNT catalyst in the HER.

Electrochemical performance

To investigate the effects of the electronic structure of IrO₂-CoPi-CNT catalysts on HER performance, the HER activity evaluation of the catalysts was performed in 0.5 M H₂SO₄ with the use of a graphite rod as a counter electrode. The performances of CoPi-CNTs, IrO₂-CNTs, CNTs, and commercial Pt/C were compared under the same conditions. The linear sweep voltammetry (LSV) curves in Fig. 3a show that IrO₂-CoPi-CNT catalysts have a much higher catalytic current density and a lower overpotential of 29 mV at a current density of 10 mA cm⁻². This result is slightly better than that of Pt/C (30 mV). Additionally, the IrO₂-CoPi-CNT catalyst has Pt-like kinetics with a Tafel slope of 27 mV dec⁻¹ towards the HER (close to the Tafel slope value of 30 mV dec⁻¹ for commercial Pt/C in Fig. 3b). These findings suggest favorable reaction kinetics of the IrO₂-CoPi-CNT catalyst and demonstrate that the HER rate-limiting step is recombination between adjacent adsorbed H atoms, which operates through the Volmer-Tafel mechanism.^{37,38} The high electrocatalytic activity of the IrO₂-CoPi-CNT catalyst toward the HER might be attributed to the synergistic interactions of IrO₂ and CoPi. For comparison, the Tafel slopes for the CoPi-CNTs (151 mV dec⁻¹), IrO₂-CNTs (119 mV dec⁻¹) and CNTs (394 mV dec⁻¹) and other specimens are shown in Fig. 3b, S1b and S2b (ESI†), respectively, which suggested that the HER process of these control samples is likely to occur by a Volmer-Heyrovsky mechanism.³⁹ The performance of the IrO₂-CoPi-CNT catalyst in the HER is compared with those of some existing catalysts in Fig. 3c and Table S1 (ESI†). The high catalytic performance of IrO₂-CoPi-CNTs with the lowest Ir loading indicates that the IrO₂-CoPi-CNT catalyst has great potential for application in the HER in acidic solution.

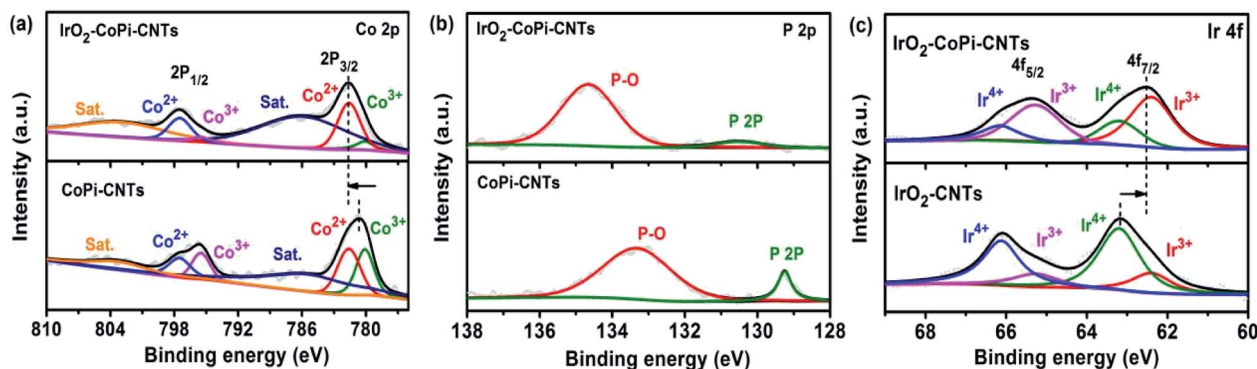


Fig. 2 Structural characterization of the catalyst: high-resolution XPS spectra of CoPi-CNTs, IrO₂-CNTs, and the IrO₂-CoPi-CNT hybrid catalyst for (a) Co 2p, (b) P 2p, and (c) Ir 4f.

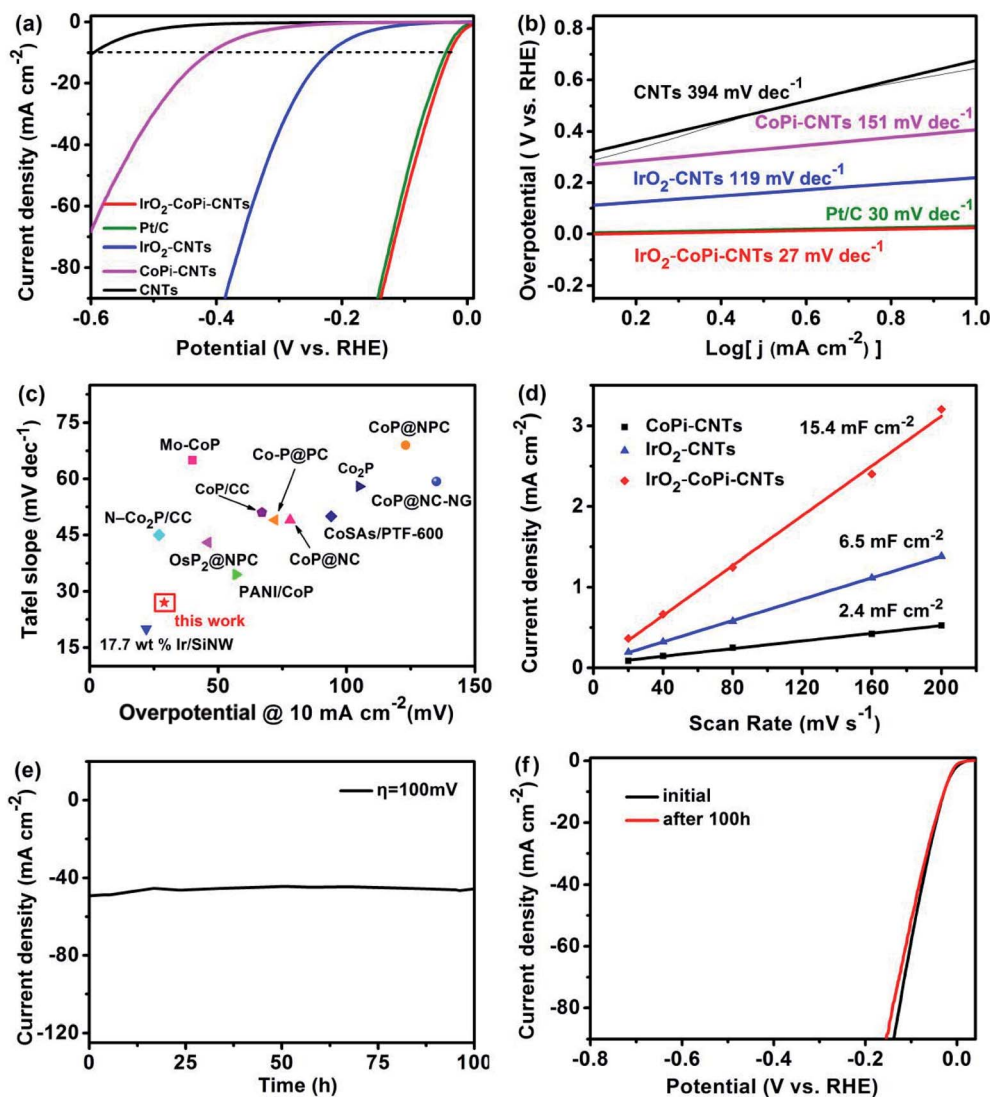


Fig. 3 HER performances of the catalysts. (a) The polarization curves for CNTs, CoPi-CNTs, IrO₂-CNTs, Pt/C, and IrO₂-CoPi-CNTs in a 0.5 M H₂SO₄ solution at a scan rate of 5 mV s⁻¹ and (b) the Tafel plots derived from the corresponding polarization curves. (c) A comparison of the overpotentials (at a current density of 10 mA cm⁻²) and the Tafel slopes for the various catalysts in the HER. Values were plotted from references (Table S1 in the ESI†). (d) Capacitive currents at 0.15 V against the scan rate and corresponding C_{dl} values estimated through linear fitting of the plots. (e) Chronoamperometry *i*-*t* curve for IrO₂-CoPi-CNTs at η = 100 mV (vs. RHE) in 0.5 M H₂SO₄. (f) LSV curves for IrO₂-CoPi-CNTs before and after 100 h.

The electrochemical surface area (ECSA) was also evaluated to understand the electrochemical performance of the catalysts in the HER.^{40,41} The ECSA values of these catalysts were measured by calculating the electrochemical double layer capacitances (C_{dl}) by CV. The corresponding standard CV curves for different catalysts at varying scan rates are shown in Fig. S8 (ESI†). A larger C_{dl} value suggests a higher ECSA. As shown in Fig. 3d, the C_{dl} of the IrO₂-CoPi-CNT catalyst was approximately 15.4 mF cm⁻², which is higher than those of CoPi-CNTs (2.4 mF cm⁻²) and IrO₂-CNTs (6.6 mF cm⁻²), indicating that the IrO₂-CoPi-CNT catalyst has a larger ECSA. This increase of the ECSA value indicates that loading IrO₂ nanoparticles onto CoPi-CNTs introduced more electrochemically active sites and increased the electrical conductivity of the catalyst, thus accelerating the overall electrocatalytic

performance in the HER. Electrochemical impedance spectroscopy (EIS) further confirmed the high catalytic activity of the IrO₂-CoPi-CNT catalyst in the HER in that this catalyst had the smallest charge transfer resistance (R_{ct}, the radius of the semicircle in the high frequency region) among all investigated catalysts (Fig. S9, and their electrical equivalent circuit diagram is shown in the inset in the ESI†). Solution resistance (R_s) corresponds to the x-intercepts at the high frequency region in Nyquist plots and the linear portion at the low frequency region represents the diffusion resistance (R_d) (impedance parameters shown in Table S2†).⁴² The large C_{dl} value corresponds to its high active surface area, which can strongly promote the HER performance. These may be the main reasons why IrO₂-CoPi-CNTs have the highest HER activity among all the catalysts.

We next examined the long-term stability of the catalysts, as shown in Fig. 3e. The current density slightly decreased after operation for 100 h at an overpotential of 100 mV vs. RHE (with a slight anodic current attenuation of 5%). Hence, the catalytic activity of the IrO₂-CoPi-CNT catalyst in the HER is highly stable. Furthermore, the polarization curve of the IrO₂-CoPi-CNT catalyst after 100 h in Fig. 3f was similar to that of the initial measurement. Moreover, the structure and morphology of the IrO₂-CoPi-CNT catalyst underwent negligible changes after 100 h testing (Fig. S10 in the ESI†). These results highlight the good durability of IrO₂-CoPi-CNTs as an efficient catalyst toward the HER.

To evaluate the inherent HER activities of the catalyst, the turnover frequency (TOF) was systematically measured in 1.0 M phosphate buffered saline (PBS, pH 7.0) (Fig. S11 in the ESI,† for details of the calculation method and experimental process).⁴³ As shown in Fig. 4a, the TOF values for CNTs, IrO₂-CNTs, CoPi-CNTs, and IrO₂-CoPi-CNTs were calculated from experimental data. From Fig. 4b, to achieve the same TOF of 0.8 s⁻¹, the overpotentials of the CNTs, IrO₂-CNTs, and CoPi-CNTs catalysts were 540, 237, and 348 mV, respectively, whereas the IrO₂-CoPi-CNTs only required 73 mV. Furthermore, we compared the TOF values of all the investigated catalysts at overpotentials of 100, 200, and 300 mV, as shown in Fig. 4c. The TOF values for the IrO₂-CoPi-CNT catalyst were consistently better than the total TOF values of CNTs, IrO₂-CNTs, and CoPi-CNTs. These results demonstrate the synergistic enhancement effects of IrO₂ cooperating with CoPi on the performance of the HER.

Microstructural mechanisms of the IrO₂-CoPi-CNT catalyst in the HER

To make clear the synergistic effects operating at the CoPi-IrO₂ interface in the HER, the key reaction steps under acidic conditions were further investigated by density functional theory (DFT) calculations. Herein, three atomic models [namely (1 × 2)-IrO₂ (110) slab, CoPi polyhedra and CoPi-IrO₂ interface] were constructed as shown in Fig. S12 and S13 (ESI†) and Fig. 5. The corresponding calculation details are shown in ESI note 1.† The stoichiometric iridium dioxide (110) surface [s-IrO₂ (110)] is one of the main facets of IrO₂.^{44–47} The reaction free energy and geometric structures of this face are summarized in Fig. S12a, b,

S13a and c–e (ESI†). The DFT calculations indicated that 5-fold coordinatively unsaturated iridium (Ir_{cus}) atoms on the s-IrO₂ (110) surface were the main active sites with a ΔG_{H*} value of −0.29 eV, which is close to the optimal Pt (111) ΔG_{H*} value of −0.08 eV. Unfortunately, 2-fold coordinated bridge oxygen (O_{br}) sites had a large negative ΔG_{H*} as low as −0.61 eV, which might hinder the diffusion of H intermediates, leading to sluggish HER kinetics. Weak chemical interactions between hydrogen adatoms and 3-fold coordinated surface oxygen (O_{surf}) sites (binding energy (ΔE_b) of +0.34 eV) disrupted the surface lattice and limited hydrogen adsorption.

For comparison, we also calculated adsorption of hydrogen on CoPi nanoclusters. A possible structural motif for CoPi is shown in Fig. S12c and d (ESI†). The Gibbs free energies and optimized geometric structures of hydrogen adsorption are listed in Fig. S13b and f–h (ESI, the corresponding results are shown in ESI note 2†). Protons are anchored onto the cluster surface at the 2-fold coordinated oxygen, 3-fold coordinated oxygen (O_{2c}, O_{3c}), and hydroxyl sites, respectively.^{36,48–50} Most of the protons tended to adsorb at the hydroxyl sites to generate H₂O molecules. These H₂O molecules decomposed because Co–OH₂ tended to oxidize and deprotonate to Co–OH and even Co=O. Adjacent O_{2c} and O_{3c} sites contributed to the migration of H* intermediates because of their moderate free energies. Hence, the CoPi nanoparticles acted as a water dissociation promoter and H* intermediate deliverer.

The complex structure formed after connecting CoPi with IrO₂ is shown in Fig. 5a. The phosphate species likely bound at the basal plane of IrO₂ (110) with one or two O–Co bonds and bridge Co-oxides and IrO₂. Notably, the projected density of states (PDOSs) of the bonded Ir_{cus} and the nearby Co and P atoms varied, as shown in Fig. 5b. This variation is related to the different PDOSs of these atoms as a function of coordination. The 2p bands of the P atoms in the CoPi-IrO₂ compound were much deeper than those of the isolated CoPi clusters and approximately 0.30 *e* transferred from P atoms to the Ir_{cus} sites. This structure prevented IrO₂ from aggregating. Because the bridged phosphates were electron-donating, the CoPi-IrO₂ compound had a much higher HER catalytic activity than that of isolated CoPi or IrO₂ catalysts owing to more thermoneutral hydrogen adsorption at the active sites. In this regard, when comparing different hydrogen adsorption sites (Fig. 5c–g), the

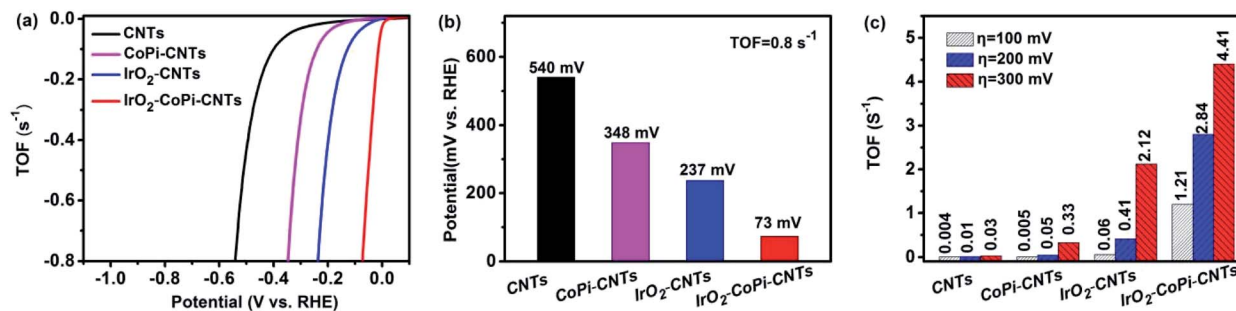


Fig. 4 The TOF values of the catalysts. (a) Calculated TOF values for CNTs, CoPi-CNTs, IrO₂-CNTs and IrO₂-CoPi-CNTs from experimental data. (b) A comparison of the overpotentials of samples at the same TOF value (0.8 s⁻¹). (c) A comparison of the TOF values of samples at various overpotentials.

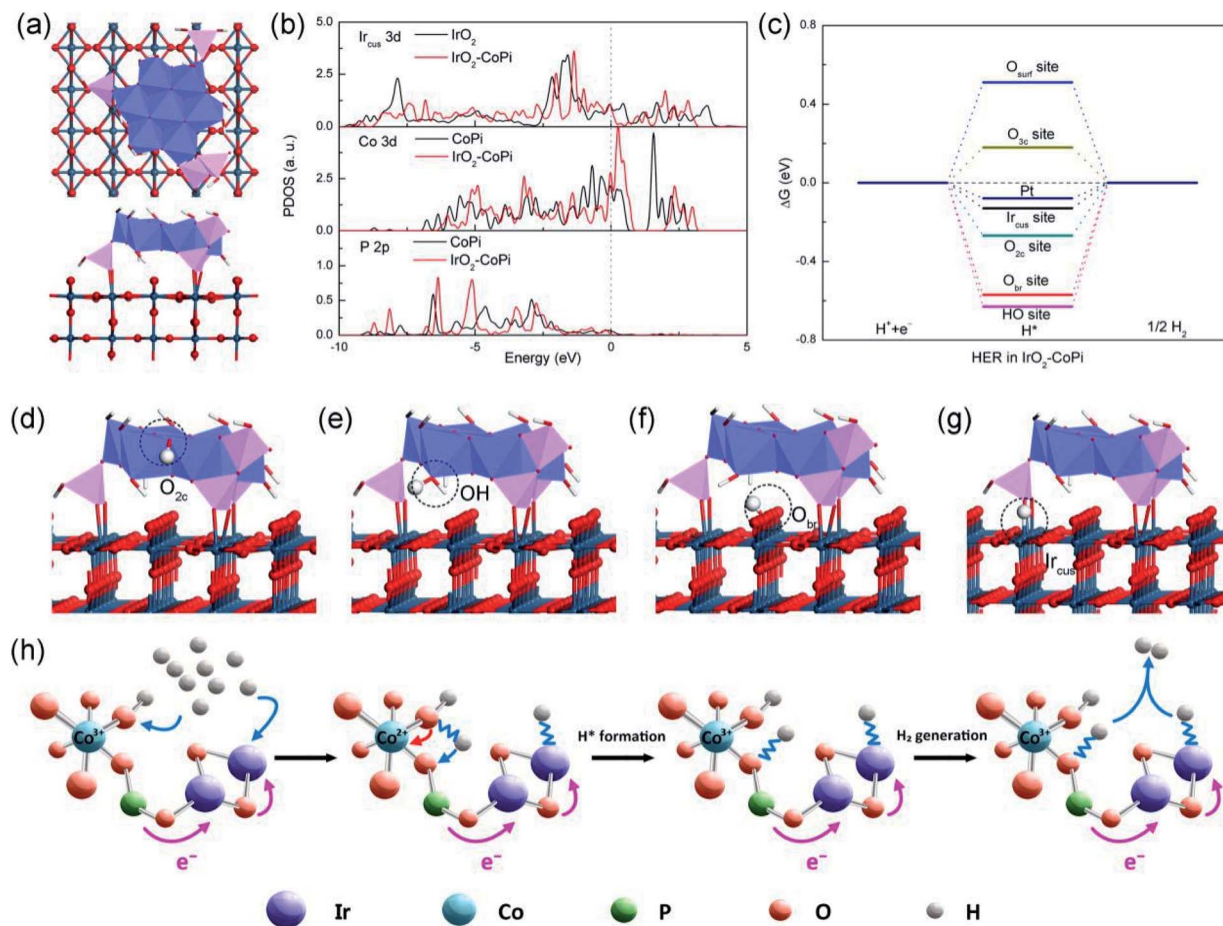


Fig. 5 DFT simulations for understanding the CoPi-IrO₂ hybrid catalyst's HER activity. (a) Top and front views of the IrO₂-CoPi complex and (b) the partial density of states (PDOS). (c) Diagram of the Gibbs free energies (ΔG) for the HER at the active sites of the CoPi-IrO₂ complex and (d–g) the binding configurations. The white, red and navy spheres are H, O, and Ir atoms, the sticks indicate H–O bonds, light blue octahedra indicate CoO₆ and pink tetrahedra denote PO₄, respectively. (h) Schematic illustration of the catalytic pathway of the CoPi-IrO₂ hybrid catalyst towards the HER in acid media.

ΔG_{H^*} for hydrogen adsorption at the nearby open Ir_{cus} sites of CoPi-IrO₂ was more favorable with an optimal value of approximately -0.13 eV. We attributed this marked change in ΔG_{H^*} to the interfacial charge transfer from the bonded phosphates to the IrO₂ substrate, modifying the surface charge distribution of their neighbors.

On the basis of the above results, according to the reaction pathway for the acidic HER [including prior H⁺ ion adsorption to form H* intermediates (Volmer step), H* diffusion or transfer at CoPi-IrO₂ interfaces and hydrogen generation (Tafel step or Heyrovsky step)], we devised a Volmer–Tafel mechanism for the reaction pathway for the acidic HER of CoPi-IrO₂ (Fig. 5h).³⁰ First, hydrogen ions are anchored onto the CoPi cluster surface at hydroxyl sites to generate H₂O molecules, which adsorbed on nearby open Ir_{cus} sites of CoPi-IrO₂ with a suitable adsorption energy. The formed HO–H on the CoPi nanoclusters effectively decomposed and offered the possibility of an abundance of H* intermediates through adjacent O_{2c} and O_{3c} site migration to nearby IrO₂ catalyst sites. The Co³⁺ sites were reduced to Co²⁺ upon hydrogen adsorption at adjacent O/OH ligands, which

then enabled the oxidation of Co²⁺ sites back to Co³⁺ upon subsequent hydrogen transfer. Finally, the H atoms combined to produce H₂ molecules. In this way, the heterostructure supported H₂ generation. This system opens the possibility of linking catalytically active complexes *via* covalent bridges in electrocatalysts.

Conclusions

In summary, we have developed a method to load IrO₂ onto the surface of CoPi-CNTs and regulate the catalyst's electronic structure to achieve Pt-like HER performance. This IrO₂-CoPi-CNT catalyst has excellent HER performance, with a small overpotential of 29 mV at a current density of 10 mA cm⁻² and a low Tafel slope of 27 mV dec⁻¹. The catalyst also has good catalytic stability in acidic media. Moreover, DFT calculations indicated that the phosphate species (P/O bridges) of the CoPi-CNTs likely connected the periphery of the Co-oxides with the IrO₂ particles to prevent their further agglomeration, which facilitated the release of the generated gas. The

XPS results confirmed that the charge transfer from Pi to the IrO₂ thus influences their intrinsic activity leading to a more optimal ΔG_{H^*} value of approximately -0.13 eV. The compound has outstanding HER performance owing to the strong synergistic effects between IrO₂ (excellent hydrogen adsorption energy) and CoPi-CNTs (rapid cleavage of HO–H bonds offering the possibility of an abundance of H* intermediates). These findings provide insight into application of Ir in the HER and a strategy for improving performance by coupling with CoPi-CNTs to form low-cost and high-performance electrocatalysts.

Experimental

Preparation of the CNT-modified electrode

Prior to coating, bare glassy carbon electrodes (GCE, 3 mm diameter) were polished using 0.3 μm and 0.05 μm alumina slurry on a piece of microcloth followed by rinsing with ultrapure water. Subsequently, the electrodes were sonicated in ethanol and dried under mild nitrogen flow. 2 mg of carbon nanotubes (CNTs, purchased from Cnano Technology, Beijing) were dispersed in 500 μL of a mixture of ethanol/ultrapure water (4 : 1, v/v) with the aid of ultrasonic agitation to form a homogeneous ink. 8 μL of the ink was dropped onto the GCE.

Synthesis of CoPi-CNT nanocomposites

The CoPi-CNT hybrid catalysts were prepared through a cyclic voltammetry (CV) electrochemical deposition method. The CNT-modified electrode as the working electrode, graphite as the counter electrode, and a saturated calomel reference electrode (SCE) were first immersed in a 0.03 M C₁₀H₁₂CoN₂Na₂O₈ aqueous solution containing NaH₂PO₄·H₂O and H₃BO₃, and then subjected to a potential cycling in the range from -1.8 to $+0.5$ V at a scan rate of 50 mV s⁻¹. The obtained CoPi-CNT modified electrode was gently rinsed with deionized water and dried under vacuum at room temperature. For comparison, parallel experiments using various deposition cycles were also carried out under the same synthesis conditions.

Synthesis of IrO₂-CoPi-CNT nanocomposites

The IrO₂-CoPi-CNT hybrid catalysts were prepared through a sacrificial counter electrode method. Typically, the electro-deposition experiments were performed in 0.5 M H₂SO₄ solution by a potential cycling from -0.6 to -1.2 V at a scan rate of 100 mV s⁻¹ using a three-electrode system consisting of the CoPi-CNT-modified working electrode, an iridium (Ir) wire counter electrode, and a saturated calomel reference electrode (SCE). After deposition, the obtained IrO₂-CoPi-CNT-modified electrode was rinsed with deionized water and dried overnight at room temperature. The parallel experiments using various deposition cycles were performed under the same conditions. For comparison, the CNT-modified GCE was used as the working electrode for the preparation of the IrO₂-CNT hybrid catalyst under the same experimental conditions.

Characterization

X-ray photoelectron spectroscopy (XPS) measurements were carried out with an ultra high-vacuum setup, equipped with a monochromatic Al K α X-ray source (10 mA, 15 kV) and a high resolution Gammadata-Scienta SES 2002 analyzer. Scanning electron microscopy (SEM) images were obtained from a JSM-6700 (spot 3.0, 15 kV). Transmission electron microscopy (TEM), high resolution TEM (HRTEM), scanning transmission electron microscopy (STEM), and energy dispersive X-ray spectroscopy (EDS) elemental mapping were performed with a JEOL-2100F instrument (200 kV). Inductively coupled plasma optical emission spectroscopy (ICP-OES) was performed on a VISTA-MPX.

Electrochemical measurements

All electrochemical measurements were performed in 0.5 M H₂SO₄ solution on a CHI760 electrochemical workstation (CH Instrument Inc.) at room temperature through a three-electrode system consisting of the catalyst-modified working electrode, a graphite counter electrode, and a KCl saturated calomel reference electrode (SCE). The SCE was calibrated with respect to the reversible hydrogen electrode (RHE) for the measurements. In our work, the potentials were obtained *versus* the reversible hydrogen electrode (RHE) through the equation $E_{\text{RHE}} = E_{\text{SCE}} + 0.267 + 0.059\text{pH}$ in 0.5 M H₂SO₄. Linear sweep voltammetry (LSV) was performed at a scan rate of 5 mV s⁻¹. The chronoamperometry curve was recorded over 100 h at $\eta = 100$ mV (*vs.* RHE). To estimate the double-layer capacitance, cyclic voltammetry (CV) was performed in the potential range from 0.1 to 0.3 V (*vs.* RHE) with various scan rates (20, 40, 80, 160, and 200 mV s⁻¹). For assessment of the HER activities of the hybrid catalysts, Tafel plots were obtained from LSV curves. According to the Tafel equation ($\eta = b \log j + a$), the Tafel slope (b) can be obtained by fitting the linear portion of the Tafel plots.¹ Electrochemical impedance spectroscopy (EIS) measurements were carried out over the frequency range from 100 kHz to 0.01 Hz at the open circuit potential with an amplitude potential of 5 mV. All data were reported without iR compensation.

Conflicts of interest

There are no conflicts to declare.

Acknowledgements

This work was supported by grants from the National Natural Science Foundation of China (51972238, 21875166, 51741207, and 51572197), Natural Science Foundation of Zhejiang Province (LR18E020001), Science and Technology Project of Zhejiang Province (LGF18B050005), and Graduate Scientific Research Foundation of Wenzhou University (3162018032). We thank Andrew Jackson, PhD, from Liwen Bianji, Edanz Group China (<http://www.liwenbianji.cn/ac>) for editing the English text of a draft of this manuscript.

References

- C. Tang, H. F. Wang and Q. Zhang, *Acc. Chem. Res.*, 2018, **51**, 881.
- H. Zhang, Z. Ma, J. Duan, H. Liu, G. Liu, T. Wang, K. Chang, M. Li, L. Shi, X. Meng, K. Wu and J. Ye, *ACS Nano*, 2016, **10**, 684.
- J. Wang, T. Ouyang, Y. Deng, Y. Hong and Z. Liu, *J. Power Sources*, 2019, **420**, 108–117.
- H. Zhang, J. Nai, L. Yu and X. Lou, *Joule*, 2017, **1**, 77.
- M. Zeng and Y. Li, *J. Mater. Chem. A*, 2015, **3**, 14942.
- P. Li, Z. Yang, J. Shen, H. Nie, Q. Cai, L. Li, M. Ge, C. Gu, X. Chen, K. Yang, L. Zhang, Y. Chen and S. Huang, *ACS Appl. Mater. Interfaces*, 2016, **8**, 3543.
- H. Zhang, P. Zhang, M. Qiu, J. Dong, Y. Zhang and X. W. D. Lou, *Adv. Mater.*, 2018, 1804883.
- Z. Liu, X. Wang, T. Ouyang, L. Wang, J. Zhong and T. Ma, *Angew. Chem., Int. Ed.*, 2019, **58**, 13291–13296.
- H. Zhang, W. Zhou, T. Chen, B. Guan, Z. Li and X. W. D. Lou, *Energy Environ. Sci.*, 2018, **11**, 1980–1984.
- T. Ouyang, Y. Ye, C. Wu, K. Xiao and Z. Liu, *Angew. Chem., Int. Ed.*, 2019, **58**, 4923–4928.
- M. Jingwen, M. Wang, G. Lei, G. Zhang, F. Zhang, W. Peng, X. Fan and L. Yang, *Small*, 2018, **14**, 1702895.
- Z. Yang, Z. Yao, G. F. Li, G. Y. Fang, H. Nie, Z. Liu, X. Zhou, X. Chen and S. Huang, *ACS Nano*, 2012, **6**, 205.
- H. Zhang, P. An, W. Zhou, B. Guan, P. Zhang, J. Dong and X. Lou, *Sci. Adv.*, 2018, **4**, eaao6657.
- H. Zhang, L. Yu, T. Chen, W. Zhou and X. Lou, *Adv. Funct. Mater.*, 2018, **28**, 1807086.
- Y. Yang, M. Luo, Y. Xing, S. Wang, W. Zhang, F. Lv, Y. Li, Y. Zhang, W. Wang and S. Guo, *Adv. Mater.*, 2018, **30**, 1706085.
- J. X. Feng, S. Y. Tong, Y. X. Tong and G. R. Li, *J. Am. Chem. Soc.*, 2018, **140**, 5118.
- I. K. Mishra, H. Zhou, J. Sun, F. Qin, K. Dahal, J. Bao, S. Chen and Z. Ren, *Energy Environ. Sci.*, 2018, **11**, 2246.
- P. Liu and J. A. Rodriguez, *J. Am. Chem. Soc.*, 2005, **127**, 14871.
- J. Shen, Z. Yang, M. Ge, P. Li, H. Nie, Q. Cai, C. Gu, K. Yang and S. Huang, *ACS Appl. Mater. Interfaces*, 2016, **8**, 17284.
- C. Tang, M. M. Titirici and Q. Zhang, *J. Energy Chem.*, 2017, **26**, 1077.
- C. Huang, Y. Zou, Y. Ye, T. Ouyang, K. Xiao and Z. Liu, *Chem. Commun.*, 2019, **55**, 7687.
- H. Zhang, W. Zhou, J. Dong, X. Lu and X. Lou, *Energy Environ. Sci.*, 2019, **12**, 3348.
- K. Wang, B. Huang, F. Lin, F. Lv, M. Luo, P. Zhou, Q. Liu, W. Zhang, C. Yang, Y. Tang, Y. Yang, W. Wang, H. Wang and S. Guo, *Adv. Energy Mater.*, 2018, **8**, 1801891.
- X. Liu, Y. Jiao, Y. Zheng, K. Davey and S. Qiao, *J. Mater. Chem. A*, 2019, **7**, 3648.
- J. Li, H. X. Liu, W. Gou, M. Zhang, Z. Xia, S. Zhang, C. R. Chang, Y. Ma and Y. Qu, *Energy Environ. Sci.*, 2019, **12**, 2298.
- P. Quaino, F. Juarez, E. Santos and W. Schmickler, *Beilstein J. Nanotechnol.*, 2014, **5**, 846.
- S. Anantharaj, S. R. Ede, K. Sakthikumar, K. Karthick, S. Mishra and S. Kundu, *ACS Catal.*, 2016, **6**, 8069.
- R. Liu, H. Zhao, X. Zhao, Z. He, Y. Lai, W. Shan, D. Bekana, G. Li and J. Liu, *Environ. Sci. Technol.*, 2018, **52**, 9992.
- J. Shan, T. Ling, K. Davey, Y. Zheng and S. Z. Qiao, *Adv. Mater.*, 2019, **31**, 1900510.
- C. Zhang, Y. Huang, Y. Yu, J. Zhang, S. Zhuo and B. Zhang, *Chem. Sci.*, 2017, **8**, 2769.
- C. Guan, W. Xiao, H. Wu, X. Liu, W. Zang, H. Zhang, J. Ding, Y. P. Feng, S. J. Pennycook and J. Wang, *Nano Energy*, 2018, **48**, 73.
- Y. Zheng, Y. Jiao, Y. Zhu, L. H. Li, Y. Han, Y. Chen, A. Du, M. Jaroniec and S. Z. Qiao, *Nat. Commun.*, 2014, **5**, 3783.
- T. Liu, P. Li, N. Yao, G. Cheng, S. Chen, W. Luo and Y. Yin, *Angew. Chem., Int. Ed.*, 2019, **58**, 4679.
- J. Wu, S. Dou, A. Shen, X. Wang, Z. Ma, C. Ouyang and S. Wang, *J. Mater. Chem. A*, 2014, **2**, 20990.
- J. Feng, F. Lv, W. Zhang, P. Li, K. Wang, C. Yang, B. Wang, Y. Yang, J. Zhou, F. Lin, G. C. Wang and S. Guo, *Adv. Mater.*, 2017, **29**, 1703798.
- M. Sheng, B. Jiang, B. Wu, F. Liao, X. Fan, H. Lin, Y. Li, Y. Lifshitz, S. T. Lee and M. Shao, *ACS Nano*, 2019, **13**, 2786.
- M. R. Chialvo and A. C. Chialvo, *Electrochim. Acta*, 1998, **44**, 841.
- M. R. Chialvo and A. C. Chialvo, *J. Electroanal. Chem.*, 1994, **372**, 209.
- Y. Yang, Z. Lun, G. Xia, F. Zheng, M. He and Q. Chen, *Energy Environ. Sci.*, 2015, **8**, 3563.
- Y. Zhan, Y. Li, Z. Yang, X. Wu, M. Ge, X. Zhou, J. Hou, X. Zheng, Y. Lai, R. Pang, H. Duan, X. Chen, H. Nie and S. Huang, *Adv. Sci.*, 2019, **6**, 1801663.
- Y. Zhan, X. Zhou, H. Nie, X. Xu, X. Zheng, J. Hou, H. Duan, S. Huang and Z. Yang, *J. Mater. Chem. A*, 2019, **7**, 15599.
- C. Huang, T. Ouyang, Y. Zou, N. Li and Z. Liu, *J. Mater. Chem. A*, 2018, **6**, 7420–7427.
- J. Tian, Q. Liu, A. M. Asiri and X. Sun, *J. Am. Chem. Soc.*, 2014, **136**, 7587.
- Y. Tsuji and K. Yoshizawa, *J. Phys. Chem. C*, 2018, **122**, 15359.
- O. Matz and M. Calatayud, *J. Phys. Chem. C*, 2017, **121**, 13135.
- M. J. S. Abb, B. Herd and H. Over, *J. Phys. Chem. C*, 2018, **122**, 14725.
- Z. Liang, T. Li, M. Kim, A. Asthagiri and J. F. Weaver, *Science*, 2017, **356**, 299.
- M. Yoshida, T. Mineo, Y. Mitsutomi, F. Yamamoto, H. Kurosu, S. Takakusagi, K. Asakura and H. Kondoh, *Chem. Lett.*, 2016, **45**, 277.
- S. Koroidov, M. F. Anderlund, S. Styring, A. Thapper and J. Messinger, *Energy Environ. Sci.*, 2015, **8**, 2492.
- M. Risch, D. Shevchenko, M. F. Anderlund, S. Styring, J. Heidkamp, K. M. Lange, A. Thapper and I. Zaharieva, *Int. J. Hydrogen Energy*, 2012, **37**, 8878.